

Supporting materials

Guoan Zheng*, Roarke Horstmeyer, and Changhui Yang

Electrical Engineering, California Institute of Technology, Pasadena, CA 91125, USA

*Correspondence should be addressed to: gazheng@caltech.edu

Supplementary Note 1: Computational cost of FPM

Assuming each captured low-resolution intensity image contains n raw pixels and we use m different LEDs for illumination, the computational complexity of the FPM algorithm can be estimated through the following steps: 1) in step 2 of the recovery process, we perform a fast Fourier transform (FFT) to generate the low-resolution image $\sqrt{I_l}e^{i\varphi_l}$. The corresponding computational cost is $n \cdot \log(n)$. 2) In step 3, we perform another FFT to update the corresponding region of the Fourier space of $\sqrt{I_{hr}}e^{i\varphi_{hr}}$. The corresponding computational cost is $n \cdot \log(n)$. 3) In step 4, the above computation is repeated for all incident angles. Thus, the total cost becomes $m \cdot 2 \cdot n \cdot \log(n)$. 4) In step 5, the entire computation is repeated r times, leading to a final computational complexity of $2 \cdot r \cdot m \cdot n \cdot \log(n)$. In our experiment, we use $r = 2$, leading to a computational complexity of $4 \cdot m \cdot n \cdot \log(n)$. Other steps during the recovery process add a negligible amount of computation time compared to the above four operations.

Supplementary Note 2: Simulations of FPM

A simple simulation clearly illustrates the principle of FPM, as shown in Fig. S1. We use a simulated object with the intensity and phase profiles in Fig. S1(a1) and S1(a2), respectively. The pixel size for the two displayed input profiles is 275 nm and the wavelength of the simulated incident illumination is 632 nm. The simulated thin object is illuminated with plane waves from 137 different incident angles, filtered by a 2X objective lens (0.08 NA) and then the field's intensity is recorded by an image sensor with 5.5 μm pixel size, which is the same as the pixel size at the image plane in our experimental setup. In this first set of simulations, we assume the sample is placed at the focal plane of the objective lens. The resulting low-resolution intensity images, with one percent random speckle noise added to each, are shown in Fig. S1(b) (9 out of the 137 total images are displayed). These low-resolution images then lead to a final reconstructed high-resolution image following the FPM's iterative recovery procedure. A maximum synthetic NA of 0.5 is achieved. Reconstructed intensity, phase, and the Fourier power spectrum are shown in Fig. S1(c). Highlighted regions in Fig. S1(c3) correspond to intensity measurements shown in Fig. S1(b).

Second, we performed a set of simulations to validate FPM's digital wavefront correction procedure in Fig. S4. The leftmost column of Fig. S4 shows 4 simulated images of an object at different locations along the axis of propagation (i.e., the z-direction). Each image exhibits a different amount of defocus aberration. Columns 2 and 3 are the recovered high-resolution intensity and phase profiles achieved using FPM's digital wavefront correction technique. Column 4 and 5 are the recovered high-resolution intensity and phase profiles without using the digital wavefront correction technique. From this comparison, we can see that the second order

defocus aberration can be compensated for up to significantly large defocus distances via wavefront correction.

Supplementary Note 3: Sampling requirement of FPM

The FPM procedure iteratively stitches together a number of low-resolution microscopy images in Fourier space to generate an accurate high-resolution image reconstruction. In the Fourier domain, we work with the complex electric field E associated with the object (its amplitude and phase are recovered during iteration, similar to phase retrieval methods). The final high-resolution reconstruction, on the other hand, is for the object intensity I ($I = E \cdot E^*$, where $*$ denotes complex conjugation). Multiplication of the electric field in the spatial domain corresponds to a convolution operation in the Fourier domain. As such, the passband of the reconstructed intensity image doubles in width in the Fourier domain. Thus, the Nyquist limit for the reconstructed intensity image pixel size becomes $\lambda/(4 \cdot \text{NA}_{\text{syn}})$ at the object plane.

Under red illumination (632 nm), this Nyquist pixel size limit is 0.37 μm . The demonstrated SBP of our FPM prototype is therefore 0.9 billion (120 mm² FOV divided by the 0.37² μm^2 Nyquist pixel area at 632 nm). In our prototype, the pixel size for each raw image is 2.75 μm at the object plane. For simplicity, we choose a reconstructed pixel size of 0.275 μm (an enhancement factor of 10), in accordance with the Nyquist requirement.

Supplementary Note 4: Estimation of pupil functions

We applied the digital wavefront correction strategy described in the text to additionally compensate for spatially varying aberrations of the employed 2X objective lens. In the following, we provide a simple calibration process for pupil function characterization (other aberration measurement techniques can also be used for this purpose). 1) We first spin coat a layer of 10-micron microspheres (Polysciences Inc.) on top of a microscope slide to create a calibration target. 2) We move the microscope stage -400 μm to +400 μm from the focal plane (50 μm per defocus step), acquiring one image of the calibration target under collimated plane wave illumination at each defocus position (17 images in total). 3) We automatically identify approximately 350 microspheres over the entire FOV of 2X objective lens using a simple digital search procedure. We choose one microsphere at the center FOV and recover its complex profile using a conventional multi-plane phase retrieval algorithm with 17 intensity measurement planes (one image for each plane). The recovered complex image of this single microsphere serves as a microsphere's "ground truth" complex field. 4) We then choose a microsphere at an off-axis position (i.e., away from the center FOV) and initialize an estimate of the pupil function at that location. Specifically, we approximate the pupil function with 5 (or more) Zernike modes, corresponding to x-tilt, y-tilt, x-astigmatism, y-astigmatism, defocus (and higher order aberrations) that may influence the point-spread function at the chosen off-axis microsphere location. We use this pupil function estimate to modify the captured 17 "ground truth" images of the central microsphere to generate a new set of aberrated ground truth defocus intensity images. We then adjust the values of the 5 (or more) unknown parameters to minimize the difference between this set of aberrated intensity images and the actual intensity measurements of the off-axis microsphere. The corresponding pupil function described by 5 (or more) Zernike modes is recovered when the mean-squared error difference is minimized. 5) Step 4 is repeated for other microspheres at different locations within the FOV. We determine each Zernike mode for approximately 350 microspheres, corresponding to 350 locations within the image. 6) Finally,

we fit these 350 values into a polynomial function $z(x, y)$, where (x, y) are spatial coordinates across the image and z denotes the amount of specific Zernike aberration at any pixel along (x, y) . This polynomial function can be used to determine a modified phase map $\varphi(k_x, k_y)$.

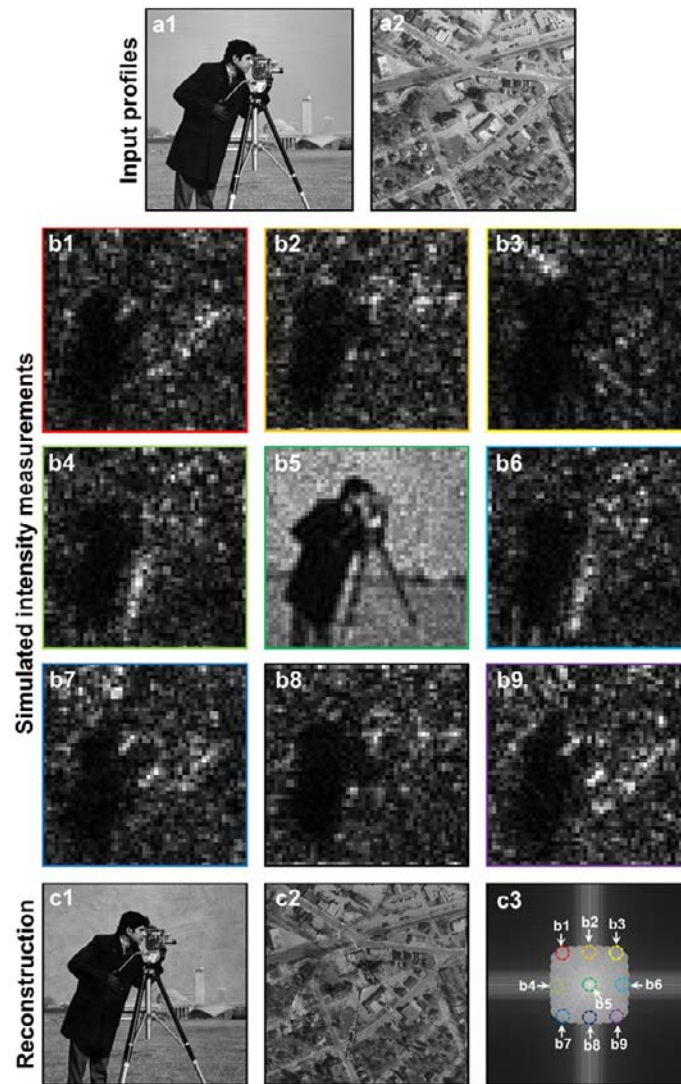


Fig. S1 Simulations of the FPM method. (a1-a2) Input intensity and phase profile of a simulated object, with a pixel size of 275 nm. (b1)-(b9) Simulated low-resolution intensity measurements of the input image (9 out of 137 are displayed), assuming a wavelength of 632 nm, a capturing NA of 0.08, and a 2.75 μm sampling pixel size. (c1-c2) The reconstructed intensity and phase images based on the simulated low-resolution intensity measurements. The pixel size of reconstructed images is 275 nm, the same as the original input. (c3) The Fourier power spectrum of the recovered complex image, displayed on a logarithmic scale. Circled regions correspond to each intensity measurement shown in (b).

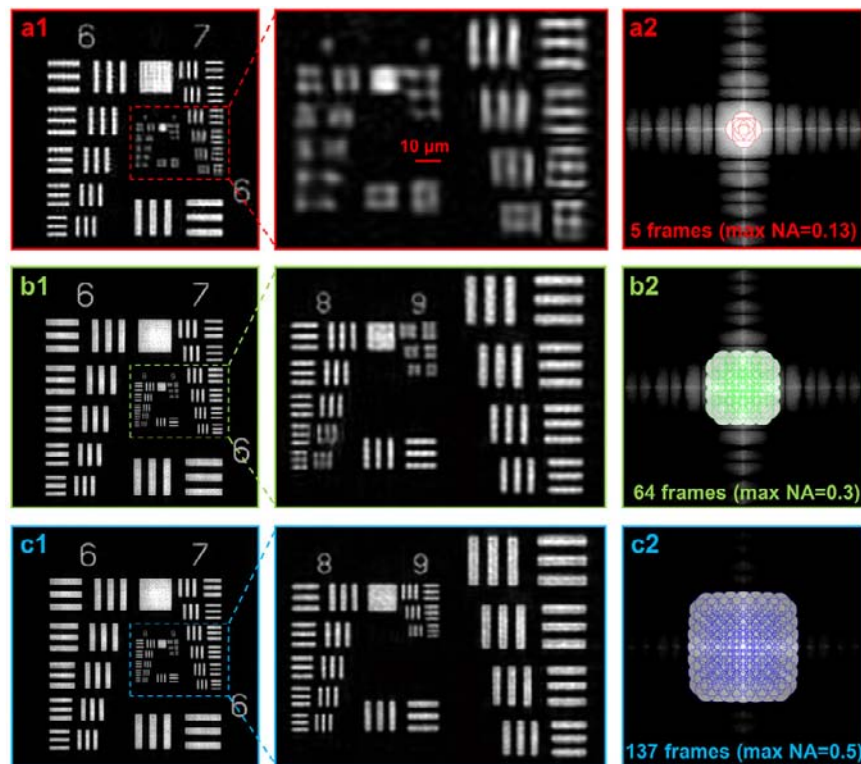


Fig. S2 FPM reconstructions using different numbers of LED light sources with corresponding Fourier power spectrums. (a) A reconstruction using 5 input images, with a maximum NA of 0.13. (b) A reconstruction using 64 input images, with a maximum NA of 0.3. (c) A reconstruction using 137 input images, with a maximum NA of 0.5. Each small circle in (a2)-(c2) represents the spectrum region corresponding to one low-resolution input image.

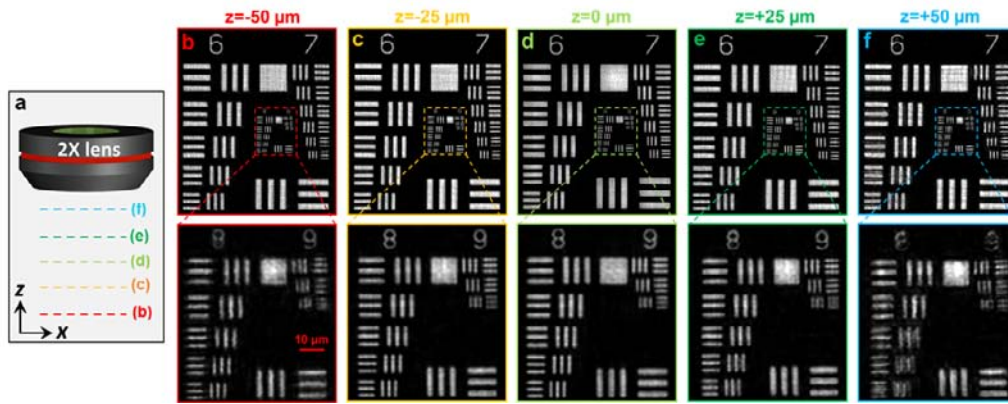


Fig. S3 Depth-of-focus characterization. (a) Experimental scheme: the USAF target is positioned at different locations along the optical axis (i.e., different z-positions), with defocus distances ranging from $-50 \mu\text{m}$ to $+50 \mu\text{m}$. (b)-(f) The corresponding FPM reconstructions from each defocus position. These reconstructions do not use our proposed digital wavefront correction procedure.

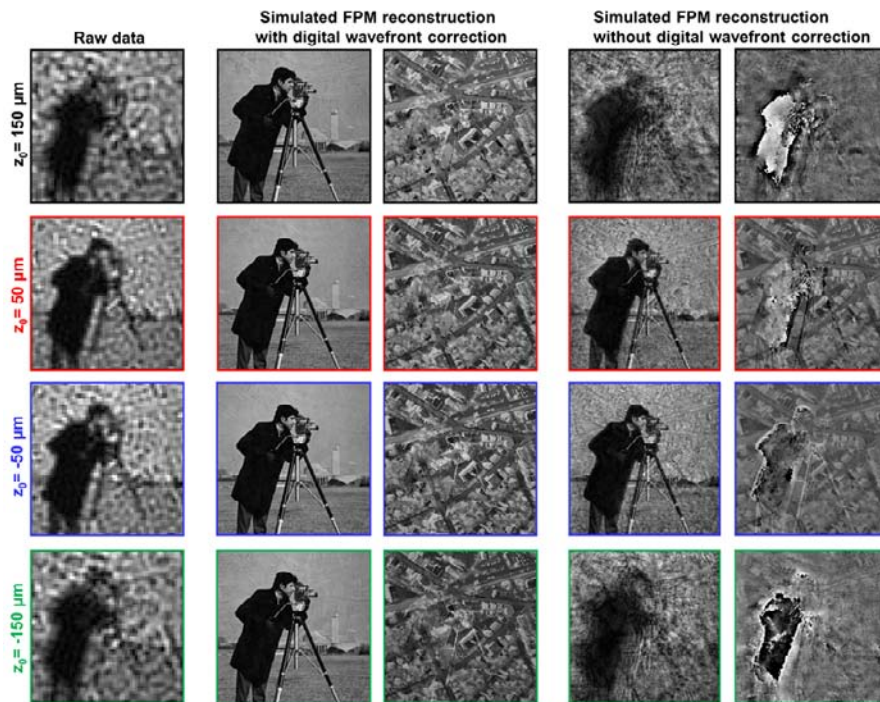


Fig. S4 Correcting aberrations with digital wavefront correction, simulation. Each row contains simulated data assuming an object at different defocus planes, ranging from $-150\ \mu\text{m}$ to $+150\ \mu\text{m}$ from the focal plane. Here, we use the same simulated object from Fig. S1. Column 1 displays one low-resolution intensity image at each defocus position. Column 2 and 3 are the recovered high-resolution intensity and phase profiles using FPM's digital wavefront correction. Column 4 and 5 are the recovered high-resolution intensity and phase profiles without digital wavefront correction, clearly exhibiting errors.

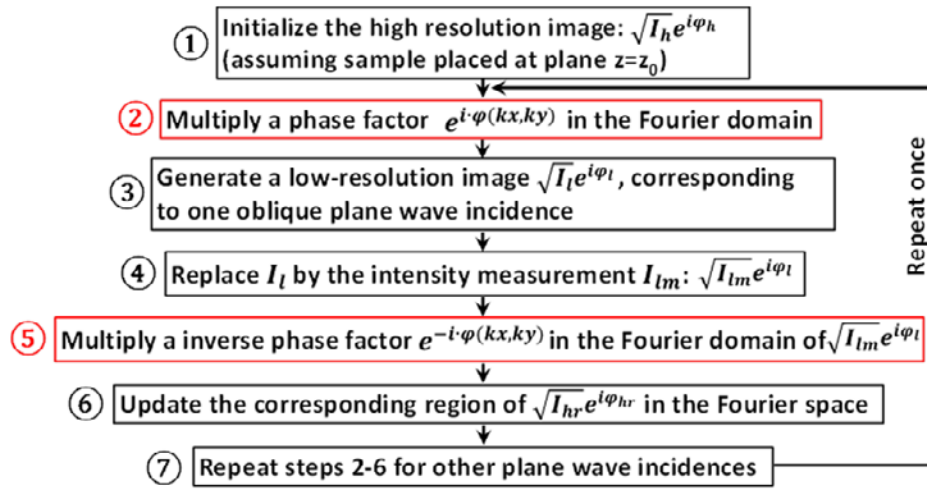


Fig. S5 FPM flowchart with digital wavefront correction. A digital pupil function is introduced in steps 2 and 5 to model the connection between the actual sample profile and the captured intensity data, which may exhibit aberrations caused by defocus.

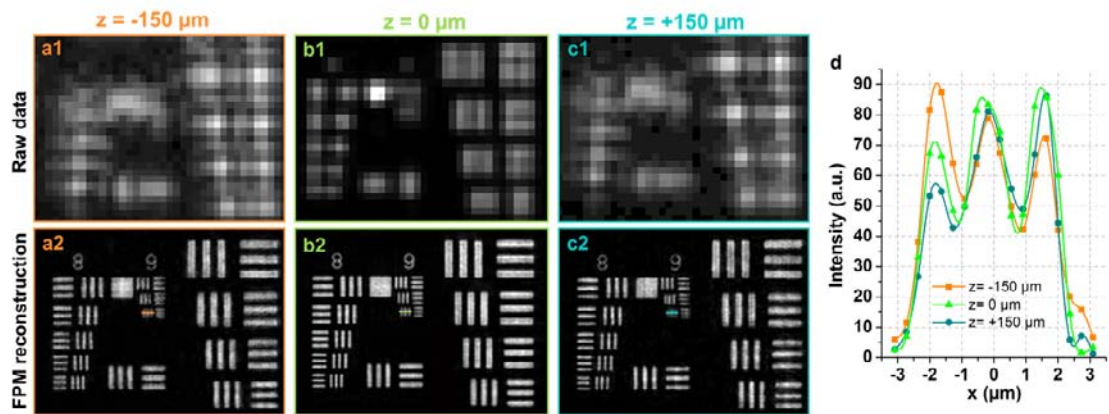


Fig. S6 Correcting aberrations with digital wavefront correction, experiment. (a1)-(c1) Low-resolution raw data of our USAF resolution target, each corresponding to different defocused distances ($-150 \mu\text{m}$ to $150 \mu\text{m}$). (a2)-(c2) FPM's high-resolution image reconstructions using digital wavefront correction. (d) Line traces for the smallest features in (a2)-(c2), with a minimum contrast difference of $\sim 30\%$.

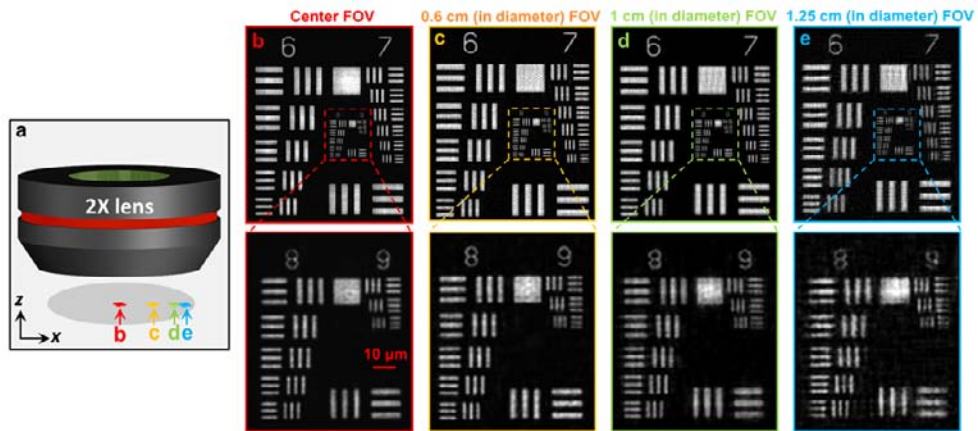


Fig. S7 Resolution enhancement across the entire image field-of-view. (a) Experiential scheme: the USAF resolution target is moved to different positions from the center to the edge of the FOV. (b)-(e) The corresponding FPM reconstructions at 0, 0.6, 1 and 1.25 cm away from the FOV center, respectively. This experiment establishes that the effective FOV of the FPM prototype is $\sim 120 \text{ mm}^2$.

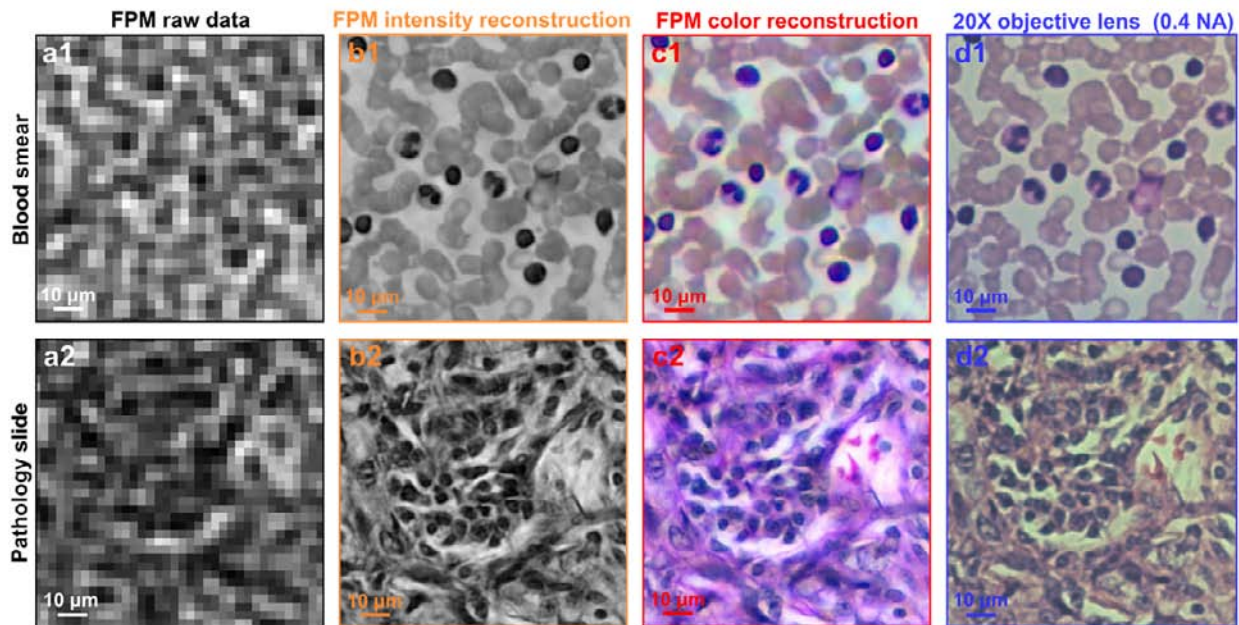


Fig. S8 High-resolution intensity and color imaging via FPM. (a) One low-resolution raw intensity image of a blood smear (a1) and a pathology slide (a2). (b) The corresponding FPM high-resolution intensity image reconstructions. (c) The same reconstructions achieved in color, using three colored wavelengths for illumination. (d) Conventional microscope images under a 20X objective lens.

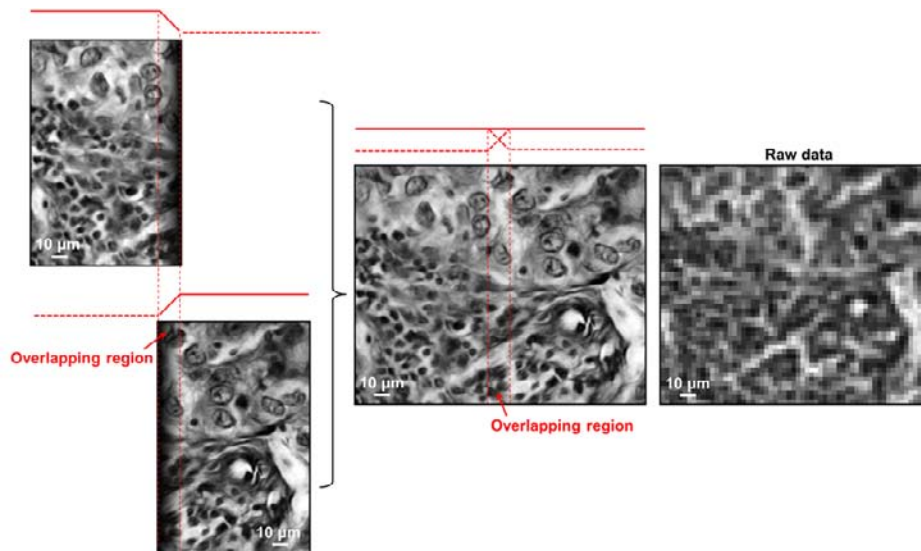


Fig. S9 Demonstration of image segment recombination. As part of our proposed parallelization of data processing, the large format raw image (5280 by 4380) is divided into smaller portions (150 by 150 raw pixels) for computation. For the reconstructed image (1500 by 1500 pixels), we cut away 50 pixels at the edge and use another 50 pixels to overlap with the adjacent portions, introducing a small degree of redundancy into our processing. Images to the left are two adjacent recovered high-resolution image segments, where their overlapping region is denoted. Images to the right demonstrate how image segments are combined using alpha blending to remove any edge artifacts. No observable boundary is present in the stitched region. This blending comes at a small computational cost of redundantly processing the regions of overlap twice.